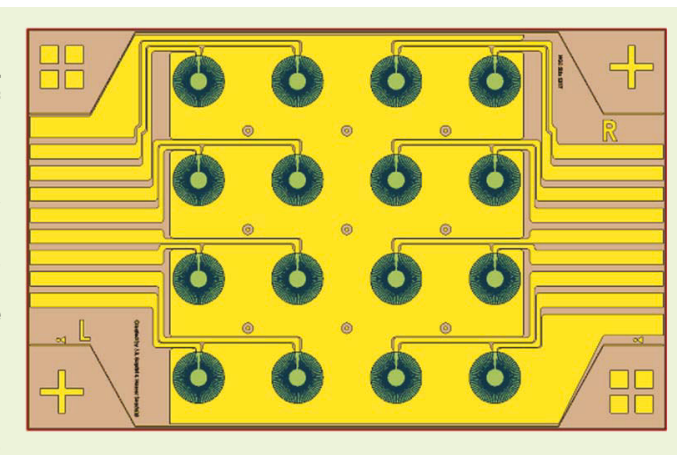


SkinCell: A Modular Tactile Sensor Patch for Physical Human–Robot Interaction

Ruoshi Zhang¹⁰, *Member, IEEE*, Ji-Tzuoh Lin¹⁰, Olalekan O. Olowo, Brian P. Goulet, Bryan Harris, and Dan O. Popa, Senior Member, IEEE

Abstract—In this article, we present the design, fabrication, integration, and performance evaluation of SkinCell sensors, a novel tactile array targeting human-robot interaction applications. A polyimide sheet is selected as the substrate of the sensor, and gold electrodes with circular interdigitated finger patterns are deposited through dc sputtering, creating a 4 x 4 sensor array with 16 tactile elements. Sensing elements are completed with a thin layer of spin-coated poly (3,4-ethylenedioxythiophene) polystyrene sulfonate (PEDOT: PSS) organic polymer solution. Two individual sensor sheets are being laminated in a back-to-back fashion to create a half-Wheatstone-bridge configuration to reduce temperature coupling while improving sensitivity. The sensor array is then sandwiched between two layers of silicone elastomer with internal dimples and cavities to improve sensitivity, repeatability, and center of force detection resolution. A COMSOL simulation was performed to study the influence of adding the



silicone encapsulation as well as design parameters to the sensor substrate. Our simulation results indicate an effective improvement of touch, i.e., voltage sensitivity by employing the featured encapsulation. Characterization experiments have been conducted to identify the sensitivity profile of each sensor on the array, which indicates an average sensitivity of 26.5 μ V/N. In subsequent experiments, the calibration profiles are used to identify the resultant force during pressing, as well as the location of the center of pressure (COP) on the SkinCell sensor. Finally, SkinCell sensors have been integrated into the OctoCan, a structural electronic device that can acquire squeezing pressure data during physical human-robot interaction (pHRI).

Index Terms—Poly(3,4-ethylenedioxythiophene) polystyrene sulfonate (PEDOT: PSS), strain gauge, tactel sensors.

I. INTRODUCTION

TUMAN skin is endowed with several neurosensory pathways that allow us to experience our environment through direct physical touch, including tactile, heat, and vibration perception. For the last 40 years, numerous researchers have studied artificial skins to endow robots with similar capabilities [1], [2], [3].

In the pursuit of engineering such sensors, touch sensing with contact force measurement is the most widely implemented due to its fundamental role during both robotic manipulations with a gripper and whole-body physical human-robot interaction (pHRI) applications [4], [5]. Typical human touch interactions will range from approximately 0.3 N (30 g/cm²)

Manuscript received 17 August 2022; revised 24 October 2022; accepted 4 November 2022. Date of publication 5 December 2022; date of current version 31 January 2023. This research was sponsored by National Science Foundation, award #1849213. The associate editor coordinating the review of this article and approving it for publication was Prof. Chang-hee Won. (Corresponding author: Ruoshi Zhang.)

The authors are with the Louisville Automation and Robotics Research Institute (LARRI), University of Louisville, Louisville, KY 40208 USA (e-mail: ruoshi.zhang@louisville.edu).

Digital Object Identifier 10.1109/JSEN.2022.3223320

for a soft stroke to more than 10 N (1000 g/cm²) for a push or slap [58]. Researchers proposed tactile sensors encapsulated in polydimethylsiloxane (PDMS) with epidermal ridges that can measure pressures ranging from 0.42 to 1.68 MPa or forces under 150 N on various depths and areas [34]. Others reported a planar tactel array made with flexible substrates capable of detecting force from 0 to 1 N [35]. A core requirement for such a sensing device is to have sufficient spatial resolution, force measurement resolution, and appropriate sensing range. The sensing mechanism directly impacts all these three goals, while the spatial resolution of the sensing device is also determined by individual sensor size and placement density. Generally, touch-sensing transducer mechanisms are based on electronic measurement of physical phenomena such as stress, strain, or proximity, transformed into change of capacitance [8], [9], inductance [10], [11], and resistance [6], [7], [12], [13]. The spatial resolution is sometimes limited by factors other than the sensing mechanism, such as interconnects from individual sensor cells to external data acquisition devices and tactile sizes [13], [14].

Pressure sensors are often used as tactile sensing, while they generally have wider applications. Two types of

1558-1748 © 2022 IEEE. Personal use is permitted, but republication/redistribution requires IEEE permission. See https://www.ieee.org/publications/rights/index.html for more information.

pressure sensors that have become commercially successful are force-sensing resistors (FSRs) and force-sensing capacitors [42]. FSRs and capacitance sensors can be fashioned into individual tactile cells for electronics hobbyists, as well as grouped into an array on the same substrate to cover a larger area for research and industrial professionals. Both types can be fabricated with flexible substrates to accommodate applications requiring mounting them on nonplanar surfaces. Biocompatible pressure sensors fabricated with MXene offer flexible and degradable wearable sensors for a wide range of applications such as health monitoring, body motion detection, and human-robot interfacing. MXene can be engineered with different compositions to be suitable for a variety of pressure ranges and spatial resolution [50], [51], [59]. Furthermore, bioresorbable pressure sensors can be implanted inside the body and resorbed after a certain time [52], [53]. Recently, a silicon-based pressure sensor implanted and later resorbed in a rat's brain has been demonstrated [52].

A different method of tactile sensing was proposed by the work in [15]. Multiple MEMS barometer sensors have been encapsulated in a molded rubber, while the rubber acts as both a soft touch interface and pressure conversion medium. Due to the small footprint, multiple MEMS sensors can be embedded under the same piece of rubber. They can be attached to robot grippers with sufficient gripper surface area, to feedback gripping force.

Recently, a new type of vision-based tactile sensing mechanism has received considerable attention. An optical rubber with engineered illumination is used as the sensing agent, and the contact-induced deformation is observed by an image sensor [16]. Different from the conventional types, vision-based sensors' force resolution is determined by an image brightness gradient, and their spatial resolution significantly increases due to the high pixel count of image sensors. They can create a delicate force map while requiring more intensive data processing, thus machine learning algorithms are often implemented to reduce computational complexity [17]. In all the above examples, design factors such as flexibility and rigidity of the sensor, transparency of the media, measurement modality, and overall composition of the sensing device dictate suitable applications [1], [18].

The SkinCell sensor in this work is introduced to address the need for large-area tactile sensorization with low costs, such as covering robot body surfaces to enable pHRI applications. Organic material poly(3,4-ethylenedioxythiophene) polystyrene sulfonate (PEDOT: PSS) was studied and reported to have favorable properties such as high gauge factor, flexibility, and good process compatibility. Depending on the composition, PEDOT: PSS as a sensing material has been reported with promising gauge factors of between 6.9 and 17.8 [31], [48] when used under strain mode and a very high gauge factor range from 396 to 12 000 when fabricated into the stretchable form [30], [54]. Due to its working mechanism, the strain-gauge sensor can precisely measure deformation, such as aircraft engine surface [19], aircraft structure crack and damage [20], static and dynamic response of bridges [21], and concrete stress of railways [22]. Many applications of straingauge sensors in the field of robotics have been implemented, such as finger-tip tactile sensing [23] and force-torque sensors placed at the base or wrist of a robot arm [24]. Straingauge-based tactile sensors utilizing metal foil elements have previously been demonstrated and investigated [41].

Successful use of spin-coated, PEDOT: PSS as a straingauge sensing element on linear interdigitated electrode (IDE) structure was demonstrated in previous work [14], [25]. Later, a design with a star-shaped IDE was proposed and studied to demonstrate sensors with omnidirectional sensitivity [26]. This type of sensor was then adopted onto a pneumatic robotic gripper to implement a model-free force controller. Experimental results demonstrate considerable improvement in maintaining delicate contact force [27]. A double-sided lamination design is proposed in [28] to address the issues related to thermal drift and improve overall sensitivity. A simulation environment, SkinSim, was proposed as a design tool to evaluate and optimize the geometry and placement of tactel sensors in pHRI applications [29]. Such applications have two major requirements. First, the sensor must be able to adapt to nonplanar surfaces. Second, the spatial resolution must be tunable, and typical resolutions needed for manipulation can be as low as 1 mm [29].

A major drawback of the previous work is related to the conversion of applied forces into strain when these sensors are encapsulated. For example, identical forces applied by indenters with different shapes will result in different strain values and, therefore, different sensor readings. In addition, when multiple strain-gauge sensors were fabricated onto one sheet of the flexible substrate nearby, the force stimulus causes the substrate wrinkles and creates undesired mechanical coupling between the sensors.

In this work, we address these challenges by sandwiching the sensor patch into soft (PDMS) encapsulations with strain concentration features, which reduces deformation coupling, levitates wrinkle propagation, and improves tactile measurement signal-to-noise ratio (SNR). The resulting sensor unit, the SkinCell, thus contains a doubly laminated 4×4 array of tactels, embedded in molded PDMS elastomer pieces. Some design highlights are discussed as follows:

- 1) Our design is allowing the sensing element and its PDMS bedding to be engineered separately, which grants higher flexibility to design sensors with different force measurement ranges—for instance, soft bedding allows weaker force measurement and vice versa, which plays a crucial role in our design. It also gives a soft touch to our sensor. We have improved the force sensing range to 2 N, and it can be engineered to a higher value by changing its stiffness, compared with [35].
- 2) Other strain-sensing tactile sensors separate the cantilever element and the sensing resistor [41], while ours combine these two and thus offer the possibility of making smaller, as well as omnidirectional sensing elements. Therefore, our tactile sensor improves spatial resolution within the vicinity of one tactel compared to traditional pressure sensors, since they require forces to be loaded evenly across the entire cell [55], [56].
- 3) The spatial resolution of our sensors is limited by the measurement noise and drift, not by the sensor geometry,

- and has been experimentally assessed to be better than 700 μ m for a sensor spacing of 7 mm and a tactel diameter of 3.65 mm.
- 4) Furthermore, PEDOT: PSS can be deposited with an aerosol jet process and used as connections and contacts [32], [60]. This process has the advantage of a large work distance of 2–5 mm and is compatible with metal nanoparticle inks, and these properties enable our sensor to be deposited onto 3-D surfaces. Compared to [41], ours have reduced fabrication complexity without using silicon bulk etching and flip-chip process and provide a higher sensor deflection range from micrometer range to millimeter range which makes it softer to touch. When the additive manufacturing process incorporates commercially available flexible printed circuit (FPC) substrates [43], this type of sensor is potentially suitable for mass production.
- 5) The resistance changes of PEDOT: PSS depends on the strain, as well as temperature changes, and a common solution for compensation of temperature drift is to include a separate unused gauge in the array. Reference [62] adds a dedicated reference nickel resistance temperature device (RTD) to each multimodal sensory unit to achieve compensation. References [35] and [57] follow a similar approach. Temperature compensation can be achieved by using a half or full Wheatstone bridge circuit [6], and in our case, a half-bridge approach is used, and the added gauge is doubling the sensitivity to strain rather than being unused.

In this article, we present the design of the SkinCell sensor, finite element analysis (FEA) studies of the proposed design, and introduce the OctoCan, as a structural electronics demonstrator for human gripping experiments. A customized force detection circuit is proposed and validated in all experiments, which has proven accurately picked up the sensor's resistance change with 24-bit resolution. SkinCell sensors are fabricated in a cleanroom with PEDOT: PSS as the active sensing material and incorporate 16 individual sensors, as a four \times four array that covers a sensing area of 28 \times 28 mm. We characterized the performance of individual SkinCell sensors with a motorized testing bench to calibrate the touch sensitivity and the spatial resolution of each sensor. Calibration data are used to determine the magnitude and the center of the loading force that has been applied to the sensing patch. A 3-D visualizer is developed to display the acquired tactile information. Finally, a finger-tip indentation experiment has conducted with the OctoCan (Fig. 1).

This article contains the following sections. Section II discusses the design details of the SkinCell sensor and Octo-Can. Section III shows FEA results. Section IV describes the SkinCell sensor's clean room fabrication steps in detail and electrical circuit development. The skin sensor calibration experiment and its setup, resolution evaluation, as well as OctoCan indentation test are presented in Section V. Section VI concludes the work and discusses future work.

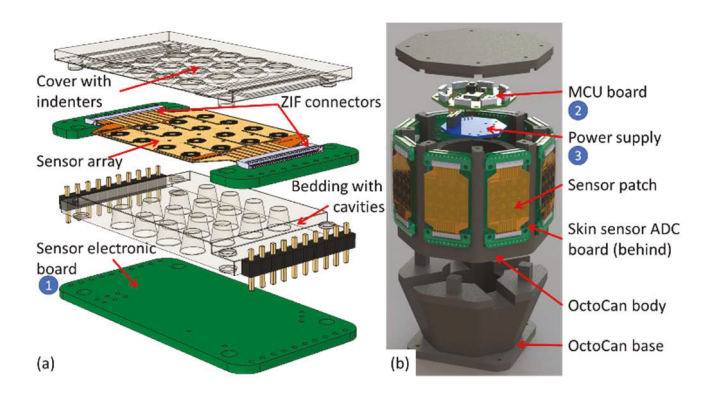


Fig. 1. Exploded view of (a) SkinCell sensor and supporting electronics (components on the other side of the PCB) and (b) OctoCan controller (FFCs are omitted).

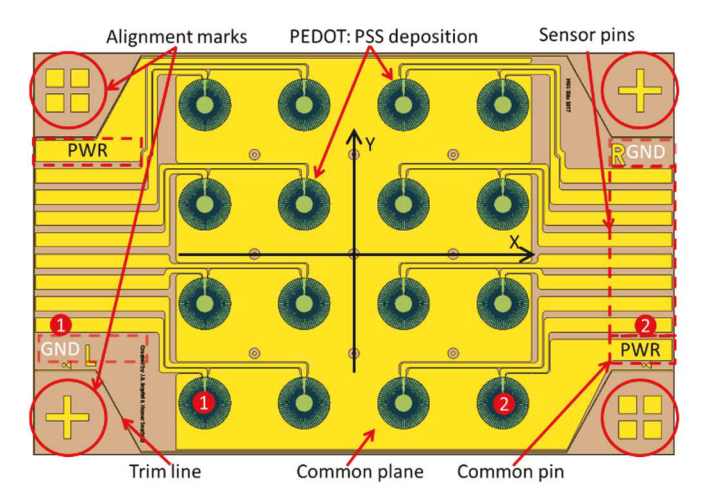


Fig. 2. Diagram of SkinCell sensor sheet.

II. DESIGN OF SKINCELL SENSOR AND OCTOCAN A. Design of SkinCell Sensor Patch

The SkinCell sensors have two functional layers with identical features, and they are assembled in a back-to-back fashion so that each sensing element on both sheets is aligned, as well as the connector pins. Fig. 2 shows the computer-aided design (CAD) drawing of an individual sheet. In this article, we refer to an individual sheet as a "sensor sheet," and an assembled and complete SkinCell sensor as a "sensor patch." Within a sensor patch, we refer to individual strain gauges on one side as "individual sensors," and each paired sensor as a "tactel."

Each sensor sheet takes a thin polyimide sheet of $50~\mu m$ as its substrate, and patterned gold is used to create positive and negative electrodes for individual sensors. The pins for electrical connection are located on both left and right edges, as well as the common pins for ground and power. A thin layer of PEDOT: PSS from Sigma-Aldrich (St. Louis, MO, USA), is spin-coated and patterned into a circular shape at each sensor site, shown as the green circles in Figs. 2 and 3. On the four corners of the sensor sheet, alignment marks are added to assist the sensor assembly process that is trimmed to

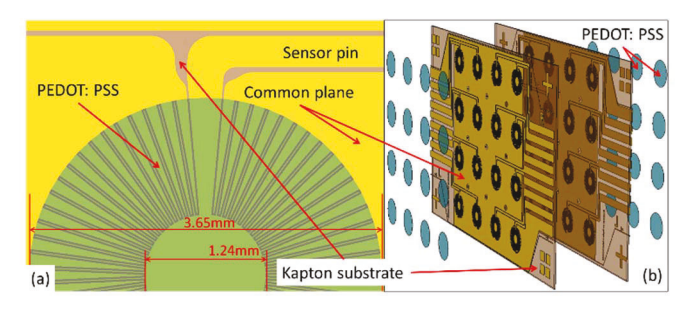


Fig. 3. (a) Dimension of an individual tactel and (b) exploded view of major components of the SkinCell sensor.

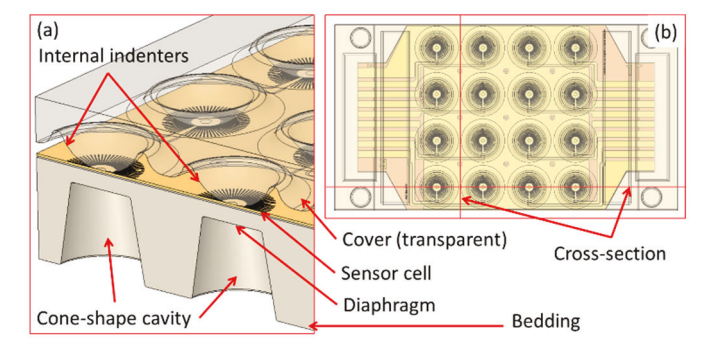


Fig. 4. (a) Cross-section view and (b) top view of a sensor assembly.

define the outline of the connectors after the sensor assembly process is done.

Fig. 3(a) shows the detail of an individual sensor, with star-shaped gauge design parameters investigated in our previous work [28]. The tactel outer and inner diameters measure 3.65 and 1.24 mm, respectively.

B. Encapsulation Design

Since each sensing element on the SkinCell sensor patch is a strain-gauge sensor and measures strain instead of contact force, thus soft bedding needs to be placed underneath each sensing element. However, if flat bedding is used, then strain response becomes indenter geometry dependent when the same force has been applied at the center of a tactel. For example, when applying pressure with the finger, the fingertip flattens when it is in contact with the sensor patch. It pushes the entire tactel down rather than strain it; hence, the sensor may fail to recover the input force. Both effects would deteriorate the spatial and force resolution of the SkinCell sensor

To clearly define the spatial and force resolution, we added cavities and spherical dimples into the silicone encapsulation. As shown in Fig. 4, the cone-shaped cavity is a structural weak point under each tactel in the bedding, which provides space for the tactel to deform and strain when force is applied. The SkinCell sensor needs to be protected from physical damage with a soft cover on top of it, which allows us to integrate a spherical dimple in it to further "focus" the strain that each tactel experiences. Thus, the sensor patch is sandwiched between the bedding and the cover. The spherical dimple

and the cone-shaped cavity together improve force-to-strain transduction, thus improving sensing repeatability [35], [41].

The cavity, sensor tactel, and dimple together can be seen and referred to as a "sensor unit." The size of each sensor unit, the distance between them, and the quantity determine the spatial resolution of a sensor patch. This design allows the sensor tactel to strain similarly regardless of the input shape, given the sensor patch closely adheres to the bedding.

Fig. 4(a) illustrates a cross section view of the bedding-sensor-cover unit. In this diagram, the cone's top and bottom diameters measure 3.16 and 4.15 mm, and 3.8-mm tall. The diaphragm under the sensor tactel is 0.7 mm thick and the sensor tactels are 7 mm away from each other. On the cover, each dimple sits in a 0.75-mm deep and 5-mm diameter recess, and it measures 4 mm in diameter from the bottom and 1.250 mm tall. A circular filet with a 2-mm radius is applied at the edge of each dimple to create a spherical surface. The choice of design parameters is simulated and discussed in Section III.

C. Sensor Detection Method

On each sensor sheet, the traces to each individual sensor are routed symmetrically according to Y-axis, so that when two sheets are assembled back-to-back; the individual sensors and their associated pins and traces are aligned. However, this arrangement does not apply to the common pins, which only appear at the top left and bottom right corners when observed in the direction shown in Fig. 2. For example, when the sheet is flipped according to the Y-axis, pin 1, and pin 2 and the tactels connected will be aligned. In this unique design, all sensor sheets can be fabricated in the same way yet properly assembled. An exploded view of the assembled sensor is shown in Fig. 3(b). When interfacing with external circuitry, two flexible flat cable (FFC) connectors with dual contact from Molex are used. Their special locking mechanism clamps the sensor contacts like a claw, which connects the top and bottom individual sensors.

Such arrangement creates a voltage divider circuit configuration on each sensing tactel where the common pins provide power and ground to the 16 pairs of voltage dividers in between. The rest of the sensor pins tap into the middle point of each voltage divider and are fed into the analog-to-digital converter (ADC). The common plane is purposely made large to reduce undesired resistance on the trace. The gold electrodes are inspired by the interdigitated finger (IDE) pattern. Instead of parallel lines in a standard configuration, we twisted the lines into a star shape. The advantage of such an arrangement is it can sense strain evenly, regardless of the location of indentation [28]. This configuration resists temperature drift as well [28].

Fig. 5 shows a circuit diagram of a sensor tactel, and it can be seen as a half-bridge circuit. R_1 and R_2 set reference voltage, and R_3 and R_4 are the active sensors. Assume $R_3 = R_4 = R$ initially, the temperature-induced resistance drift ΔR can be canceled according to equation (1), given that

¹Registered trademark.

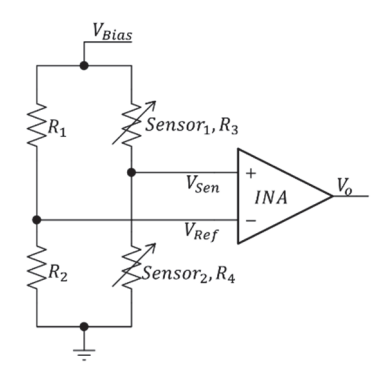


Fig. 5. Illustration of sensor patch measurement circuit.

 R_3 and R_4 experience similar temperature changes

$$V'_{\text{Sen}} = V_{\text{Bias}} \cdot \frac{R + \Delta R}{2(R + \Delta R)} = \frac{1}{2} V_{\text{Bias}}.$$
 (1)

Compared to a quarter-bridge configuration, a half-bridge can boost the sensitivity by approximately a factor of 2, assuming the bridge is balanced under $R_1 = R_2$, $R_3 = R_4$, and strain ε induces the same ΔR to R_3 and R_4 with opposite sign

$$|V_{\text{Sen}} - V_{\text{Ref}}| = V_{\text{Bias}} \cdot \left| \frac{R_4}{R_3 + R_4} - \frac{R_2}{R_1 + R_2} \right|.$$
 (2)

Equation (2) describes the general relation between resistors and the voltages, and ΔR can be expressed in the following equation:

$$\Delta R = R_G \cdot k \cdot \varepsilon \tag{3}$$

where k is the gauge factor of the sensor and R_G is the base resistance of the gauge. Equation (4) indicates strain ε induced $V_{\rm Sen}$ change with respect to half-bridge configurations

$$|V_{\rm Sen} - V_{\rm Ref}| = V_{\rm Bias} \cdot \left| \frac{k \cdot \varepsilon}{2} \right|.$$
 (4)

 $V_{\rm Bias}$ is generated by a voltage divider circuit with high precision resistors and buffered by an operational amplifier (Op-Amp) voltage buffer to create 26 mV with an adequate current to supply all 16 sensor tactels. The reference voltage $V_{\rm Ref}$ is generated similarly from $V_{\rm Bias}$ with R_1 and R_2 depicted in Fig. 5 and buffered by an Op-Amp. $V_{\rm Bias}$ is set to be two times of $V_{\rm Ref}$, based on the assumption of all individual sensors have about the same resistance value. The voltage difference between $V_{\rm Sen}$ and $V_{\rm Ref}$ is fed into an instrument amplifier with a gain of 30, and then digitized by a high-precision ADC. A microcontroller unit (MCU) is implemented to coordinate the analog-to-digital (A/D) conversion of all sensor tactels and data communications to the person computer (PC).

Implementation details of the circuit are discussed in Section IV-C.

D. Data Collection Firmware of OctoCan

The OctoCan controller shown in Fig. 1 is designed to integrate several SkinCell sensors in a pHRI application. Eight slots on OctoCan's surface are created to accommodate eight encapsulated SkinCell sensors. Each sensor carries a dedicated circuit board to perform A/D conversion. Fig. 1(a) shows an

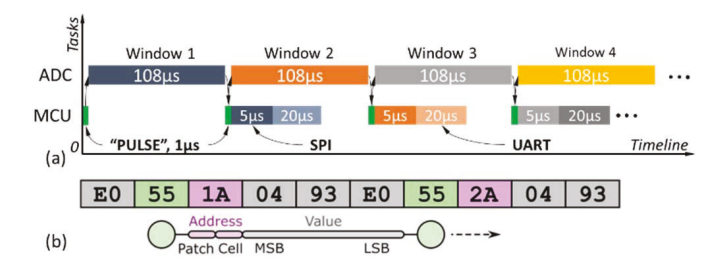


Fig. 6. (a) ADC and MCU tasks of the OctoCan electronics. (b) Format of a data package.

exploded view of a complete SkinCell sensor and its circuit board, while the OctoCan is shown in Fig. 1(b), which consists of a detachable base that can be screwed onto a surface and the body with eight sensors. A detailed description of electronic construction can be found in Section IV-C.

Customized firmware is implemented to collect data from all eight sensor patches in a round-robin fashion. The MCU talks to each ADC through the serial peripheral interface (SPI) bus and communicates with a PC through a universal asynchronous receiver/transmitter (UART) to universal serial bus (USB) dongle. A/D conversion, SPI communication, and serial transmission rates are all configurable through registers.

The OctoCan electronics executes two major tasks: 1) the ADC task: to digitize sensor readings and 2) the MCU task. The latter can be further divided into three subtasks, to commence A/D conversion by sending a "pulse" command to each ADC, to collect data from ADC, and to forward the converted data to the PC for visualization and processing. Thus, two timelines are used to represent the two tasks, as shown in Fig. 6(a). There are eight SkinCell sensor patches attached to one OctoCan; hence, eight ADC chips are used. To guarantee conversion accuracy, each A/D conversion requires 108 µs to finish a sample and conversion cycle. Since it is the most timeconsuming task, the timeline is divided based on it. The ADCs are numbered $1, 2, 3, \ldots$, and 8, and each one corresponds to a time window. The ADC task and the MCU task are parallelized to improve the overall sampling rate, where the MCU collects digitalized data from ADC(n) and forwards it to the PC at the window (n + 1). In Fig. 6(a), the green blocks represent a "PULSE" command that commences an A/D conversion, and then the MCU collects data from ADC which needs 5 μ s from the SPI interface. Eventually, it takes 20 μ s to forward the data to the PC through the UART port. For instance, ADC(1)'s data are picked up and transmitted in the window (2). The theoretical data rate of the OctoCan with eight sensor patches can be determined by each $(108 + 1) \mu s$ window, which can be calculated from the following equation:

DataRate =
$$\frac{1}{(T_{\text{converstion}} + T_{\text{PULSE}} \times 16 \times 8)}$$
 (5)

where $T_{\rm conversion}$ is the time the ADC needed to conduct A/D conversion, and $T_{\rm PULSE}$ is the time of a start conversion command. Our current data rate is 71.7 Hz.

Each UART data packet needs to be addressed individually when being sent to the PC. We name sensor patches (P) from 1 to 8 (0 \times 08) and sensor tactel (T) on each patch as 0–15 (0 \times 0F), so they can be assembled into one byte.

For example, the 11th sensor tactel on the 1st sensor patch is named "(P1 TA)"; thus, it has an *address byte* of $0 \times 1A$. The entire 128 sensor tactels are scanned in the following sequence: (P1 T0), (P2 T0), (P3 T0), ..., (P1 T1), (P2 T1), (P3 T1), until (P8 TF), all digits are *hexadecimal*. We add a *starting byte* of 0×55 at the beginning of each data packet to help align the communication between the MCU and the PC and followed by the *address byte* and three bytes of ADC data. As shown in Fig. 6(b), which represents the 1st patch, the 11th tactel has a reading of $0 \times 0493E0$.

III. FINITE ELEMENT ANALYSIS

In this section, the simulation results of the sensor with PDMS encapsulation are presented and discussed. These results provide more detail than the previous models that partially characterized SkinCell in our paper [28].

A. Simulation Setup

PEDOT: PSS is often used for its mechanical flexibility and electrical conduction and is considered one of the most successful intrinsically conductive or semi-conductive polymers (ICPs) [44], [45]. ICPs are conductive due to the presence of conjugated double bonds [44], thus giving rise to conjugated π -electrons [44], [45]. The piezoresistive properties of PEDOT: PSS depend on the change in geometry, such as inversely proportional to the length and the proportional to the area, or the interaction between the polymer and fillers particles from the modification of strain, or both effects [45], [46]. The PEDOT: PSS material was modeled in FEA multiphysics tools using p-type silicon with empirical transverse and longitudinal piezoresistive coefficients of 4.6 e^{-10} and -7.1 e^{-10} $m^4/(s \cdot A^2)$, which are based on measurements from a PEDOT:PSS sample of 1 \times 10 \times 0.2 mm under bending experiment from our bench test. The number density is $8.86 e^{15} \text{ cm}^{-3}$ for the piezoresistive value which is implemented in COMSOL¹. The sensor's gauge factor depends on the stretchability of the substrate [47]. Since the same silicone substrate is used, the sensor's gauge factor is assumed to be independent of the sensor's thickness. To avoid a high aspect ratio in the meshing that leads to divergence and prolonged simulation time, a 3- μ m thickness of the PEDOT: PSS and gold electrodes is used in the simulation. The resistance value of the model is extrapolated to be 4 Ω at 150 nm of the PEDOT: PSS, compared to the measured average value of 30 Ω . The discrepancies come from the uneven thickness of the PEDOT: PSS and the variation of the contact resistance between PEDOT: PSS and gold.

The bedding material involved is a type of PDMS, commonly known as silicone with the commercial name Sylguard 184. The Young's modulus of the silicone is 2.2 MPa when cured at 125 °C [33]. The simulations include the skin patch and its encapsulation, both of which complete the skin sensor package. The encapsulation is comprised of a cover and bedding that would provide conformance for strain transfer from external force to the sensor cell. The cover is equipped with discrete indenting bumps, which transfer and concentrate forces to the sensitive location of the tactile sensor

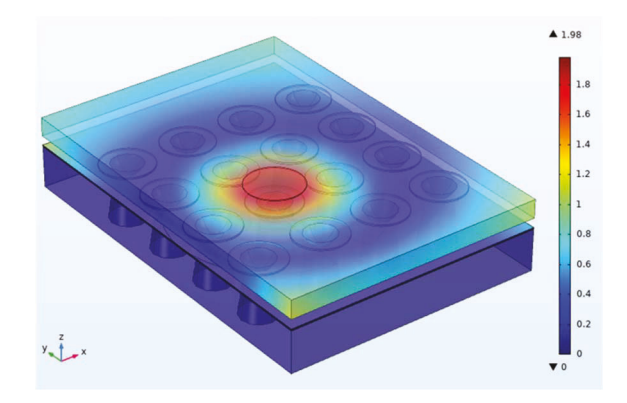


Fig. 7. COMSOL simulation of input force on top of one sensor unit.

[34], [35], [36]. The force applied on the encapsulation that sandwiches the sensor patch is shown in Fig. 7.

In contrast, the bedding is hollowed with cavities to provide location-sensitive membrane that is aligned with the center of the sensor and the indenter above. The geometry of an individual sensor and the dimple is arranged so the force is redirected from the cover through the dimples to the most sensitive area of the sensor where the maximum stress is applied, and the strain is induced.

B. Simulation Results

The simulations yield three important insights for the integration of the sensor and the encapsulation, including 1) the effect of varying indenter size; 2) the effect of a back-to-back lamination of the SkinCell sensors; and 3) the effect of the inclusion of bottom cavities.

The measured sensitivity of the SkinCell depends on the size and location of the force contact point through an indenter. Taking the center of a sensor tactel as the reference, the smaller the indentation size, we expected the more sensitive the sensor will be to equal sensor application forces applied vertically on the sensor.

In the first set of simulations, only one single layer of sensor and flat bedding without cavities were used. For a fair comparison of the indentation size as a variable, a constant 2 N force is applied to a 5-mm diameter circle on the cover, simulating the force from the size of a fingertip, which applies to all following simulations. We observed the sensitivity peaked as the dimple at a size of 4 mm in diameter. The results are shown in Fig. 8, in which the red dots represent simulation results, and the blue curve is interpolated by MATLAB's "pchip" method. In the figure, there is an increase of sensitivity of 138% with the dimple diameter at 4 mm compared with 6 mm. Furthermore, when the dimple size increases to 8 mm and beyond, the sensitivity reduces to the noise level.

For a temperature-sensitive tactel such as ours, due to the organic PEDOT: PSS material [37], temperature compensation is necessary. Therefore, two layers of the sensor with similar resistance are attached back-to-back for temperature compensation [28]. In the following simulation, the two layers of the laminated sensor are connected in series in a half-bridge configuration. Results in Fig. 9 show that the collective

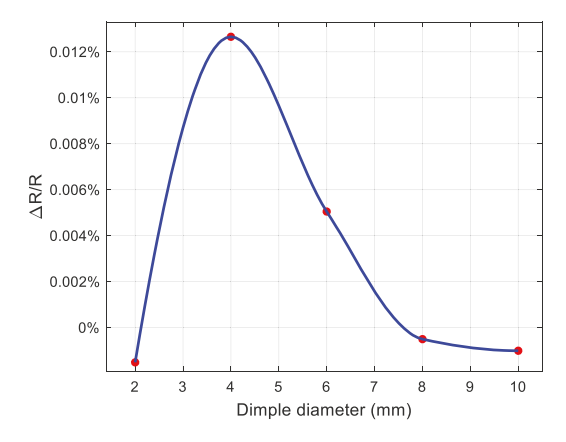


Fig. 8. Dimple size and sensor unit sensitivity with 2-N input force.

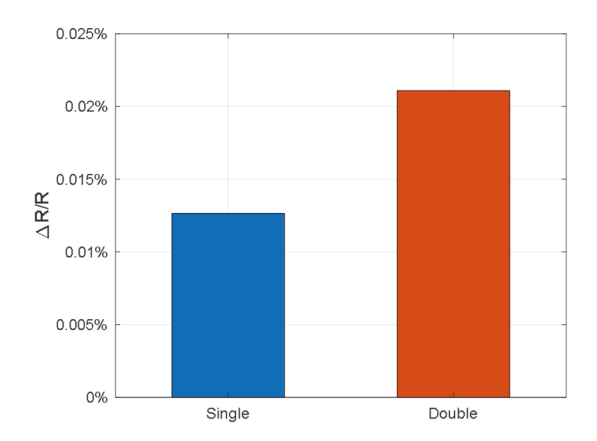


Fig. 9. Sensitivity comparison between single- and double-layer sensor units

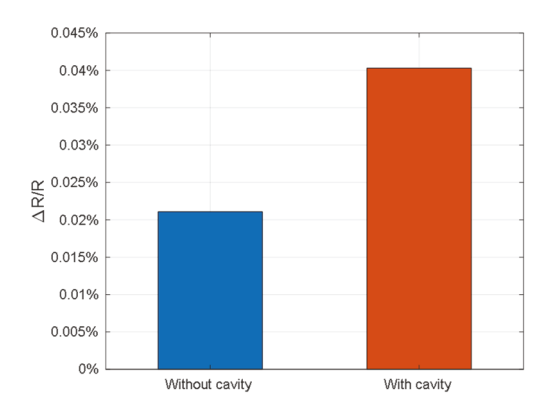


Fig. 10. Sensitivity comparison between sensor units with and without a cavity.

resistance changes in this configuration increase by 67% when compared to a single-layer sensor, because the resistance on the top layer increases and the bottom resistance decreases due to tension and compression, respectively.

In the third simulation, we compared the sensitivity of the sensor on the bedding with or without a cavity. Fig. 10 shows the sensitivity comparison between sensors with and without a bedding cavity. The cavity helps the sensor get displaced and stressed more because of the thinner membrane the sensor sits

on. The sensitivity indeed increases by 91% when the bedding is fit with a cavity than there is no cavity.

In summary, a desirable indenter's size has been found so the finger touch is sensitive enough that a further increase of the sensitivity is possible. In our PEDOT: PSS sensitivity benchmark experiment, we also observed nonlinear sensitivity, which increases under prestressed conditions. Our simulations are about ten times less sensitive than was observed in our experiments, possibly attributed to the prestress condition of the PEDOT: PSS film, which was deposited on the stressed Kapton over silicon wafer subjected to elevated processing temperatures and later peeled off from the substrate at room temperature.

IV. SKINCELL SENSOR FABRICATION AND ELECTRONICS ASSEMBLY

The SkinCell sensors are fabricated on a Kapton¹ polyimide substrate by a well-developed fabrication technique in the cleanroom. Once the individual sensor sheets are created, they are carefully aligned and laminated, and ready to be tested. Dedicated electronics-supporting board is assembled for each SkinCell sensor patch, which will be discussed in this section as well.

A. SkinCell Sensor Fabrication

The fabrication process starts by adhering the polyimide substrate to a silicon carrier wafer. A 50- μ m-thick polyimide sheet is cut in the appropriate size to match a 4" carrier wafer. It is cleaned with acetone and isopropyl alcohol and dried with compressed nitrogen to remove dirt and dust particles from the surface. The cleaned sheet then adheres to the carrier wafer which is spin-coated with a photoresist (Shirley 1813) at 3000 RPM for 30 s and baked under 115 °C for 90 s. Then, the polyimide sheet is smoothened out with a brayer roller to remove air bubbles trapped underneath [38], [39], [40].

A 300-nm gold layer is deposited and patterned to create sensor electrodes, contact pads, and traces. The gold sputtering process is conducted with a Lesker¹ PVD75 sputterer with approximately 1.6×10^{-6} Torr background vacuum, 5mTorr of Argon base pressure, 300 W of dc power, and 3.5 min of sputtering time. The design patterns are masked by Shipley¹ 1813 photoresist and etched by gold etchant (GE-8111 from Transene Company, Inc.). The patterned features are inspected under a microscope and short-circuit problem was examined with a multimeter to evaluate cleanroom fabrication yield.

The PEDOT: PSS obtained from Sigma Aldrich has a high gauge factor [48]. The one reported in this article is 5.0 wt.% concentration, 1.5–2.0 PH, approximately 50 000-mPa \cdot s viscosity at 20 °C, and 130- Ω /sq average sheet resistance.

The PEDOT: PSS layer needs to be deposited and patterned on top of the gold electrodes. To improve the wettability and spin-coating compatibility, every 0.77 g of stock PEDOT: PSS is mixed with 2 g of dimethyl sulfoxide (DMSO) and 2 g of polyvinylpyrrolidone (PVP). The resulting PEDOT: PSS colloidal solution is spin-coated on the patterned polyimide substrate at 3000 RPM for 30 s. A protective layer of parylene is deposited on top of PEDOT: PSS to shield

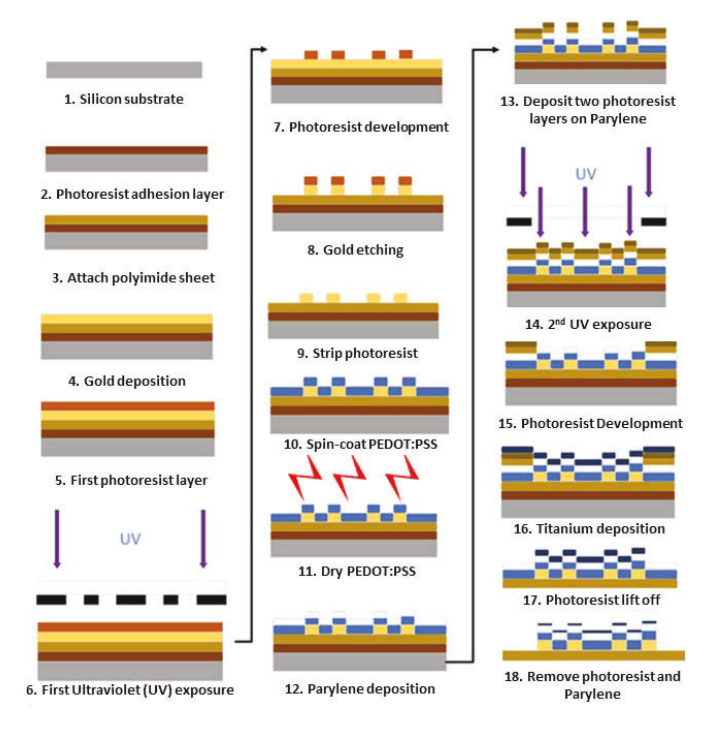


Fig. 11. SkinCell sensors cleanroom fabrication procedure.

atmospheric moisture, by vapor deposition with the SCS Labcoter¹ 2 Parylene Deposition System. Eventually, a titanium layer is deposited and patterned on top of each tactel with a lift-off process to create a etch mask for subsequent dry etching, which removes the PEDOT: PSS and parylene [39] from the undesired surface. Fig. 11 illustrates the cleanroom fabrication process.

B. SkinCell Sensor Lamination and Assembly

SkinCell sensors are laminated between Kapton sheets to protect the sensor features from mechanical wear and to shield them from atmospheric humidity. Then, the individual sheet must be bonded back-to-back to create a fully assembled sensor patch. This process enables the voltage divider configuration mentioned in Section II-C [25], [38]. According to our previous study [28], the double-sided laminated design, along with a well-matched resistance of the sensor pair, significantly reduces the temperature drift of our SkinCell sensors when compared to single-sided array designs. Section II-C further discusses this aspect.

The resulting sensors are then trimmed to expose connector pins on both sides of the SkinCell patch. A completed SkinCell sensor patch is shown in Fig. 12(a).

The sensor's bedding and cover are created from silicone rubber using a molding process. SYLGARD¹ 184 Silicone Elastomer from Dow Chemical Inc. (Midland, MI, USA) is selected due to its desired properties, such as transparent finish to achieve better sensor-to-silicone alignment, long working time, controllable viscosity, elevated curing temperature, appropriate stiffness, and good dielectric property. The two-part molds are 3-D printed by a stereolithography (SLA) printer (Formlabs¹ Form 2) and polished before use. The elastomer base and curing agent are mixed in a 10:1 ratio by volume in a mixing cup and stirred vigorously for 10 min

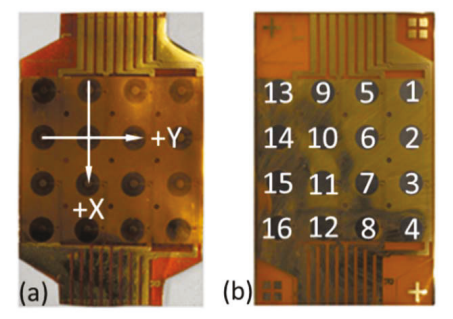


Fig. 12. (a) Laminated sensor patch and (b) individual sensor sheet. The marked tactel in (a) is used to conduct spatial resolution evaluation in Section V-B. (b) Numbering of each tactel.

to achieve even mixing. The compound is then degassed in a vacuum chamber until no more bubbles emerge from the liquid. The molds are treated with a mold release agent (Ease Release² 200) and tightly assembled. The silicone is carefully and slowly transferred into the mold by a syringe to avoid trapping air. The silicone is cured in a preheated scientific oven at 60 °C for 24 h.

C. Electronics Development

Three types of customized PCBs are developed to carry out sensor data collection and transmission tasks: 1) the sensor electronic board; 2) the MCU board; and 3) the power supply board (all marked in Fig. 1).

The 1) sensor electronic board performs A/D conversion for all 16 tactels. It features a 24-bit, 16-channel ADC ADS1258 [Texas Instruments¹, (TI)] and its supporting circuits. An instrument amplifier INA333 from TI is chosen to amplify $|V_{Sen} - V_{Ref}|$ signal, where the V_{Sen} and V_{Ref} are generated by an Op-Amp OPA1612 from TI as well. Two low-dropout (LDO) regulators of TPS7A49 and TPS7A39 from TI are added to create a low-noise, ± 2.5 -V bipolar dc power supply dedicated to the analog portion of the ADC and the amplifiers. Another LDO TPS73433 from TI is dedicated generate digital power for the ADC. An FFC connector (Molex¹, 52559-1052) is attached to conduct data communication and receive ± 5 V power for the LDOs. On the other side of the board, two FFC connectors (Molex¹, 503480-3200) are located on the left and right sides to interface with the sensor patch.

On the 2) MCU board, dsPIC33EP512MC806 from Microchip Technology is chosen for its abundant I/O capability, balanced performance, and simplicity to use. Eight FFC connectors (Molex 1 , 52559-1052) are attached to this board to connect the serial communication ports between the ADCs and the MCU, as well as to supply ± 5 V to each sensor electronic board.

The 3) power supply board is attached to the back side of the MCU board through headers, and it takes barrel jack power connectors to receive dc power. A 3.3-V LM1117 from TI¹ is used to generate the power supply to the MCU. The MCU's UART TX and RX pins are also routed to this board so that they can be connected to the UART to USB dongle, such as modules that feature FT232 from FTDI¹.

Boards 2) and 3) are located inside the OctoCan, as Fig. 1 demonstrates.

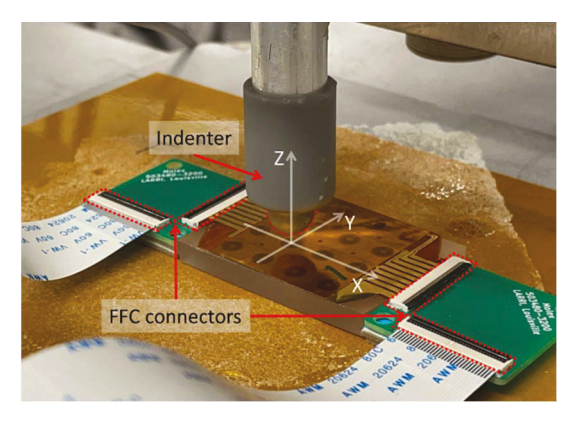


Fig. 13. Illustration of SkinCell sensor calibration experimental setup. (Sensor top cover not shown).

V. EXPERIMENTAL RESULTS

Individual SkinCell sensors are evaluated under a customized automatic indentation testing bench for performance examination and individual sensitivity profile characterization. Details of the implementation of the testing bench can be found in [28]. We apply different sets of static or dynamic forces with a 3-D-printed indenter in a direction perpendicular to each tactel and traversed all units on the sensor patch. Sensor readings are then collected and processed to calibrate all sensitivity profiles, compute the resultant forces and location of the pressure center, and determine the spatial resolution of the sensor. Finally, we demonstrate mounting the sensor patches on the OctoCan to conduct human finger indentation experiments.

A. SkinCell Sensor Force Calibration

To interpret voltage measurements into force values comparable between sensor tactels, raw ADC voltage values from each sensor tactel must be individually calibrated. Calibration compensates for variations in the manufacturing of tactels, which may cause differences in resistance values for similar strains. During this step, the OctoCan MCU transmits complete raw ADC readings of voltage over the serial interface to the host computer without any preprocessing. We wrote a high-speed multi-threaded serial communication tool for Linux in C that processes raw ADC readings for calibration and smoothing. Through a Python extension, the in-memory data structures are also exposed for simple visualizations of live data.

In the test, an encapsulated SkinCell sensor was attached to the motorized X-Y stage of our experimental indenter for raster scanning. An indenter tip with a load cell sensor was mounted to a motorized Z stage to apply force onto each tactel. The indenter was covered by a 3-D-printed spherical tip. Initial alignment was done visually, but the rest of the indentations are collected automatically by raster scanning. A close-up look at our experimental setup can be seen in Fig. 13.

The calibration experiment sequentially presses each tactel while recording the force applied by the indenter onto the sensor and the stream of raw ADC voltage measurements. Temporal information of the force must be identified to

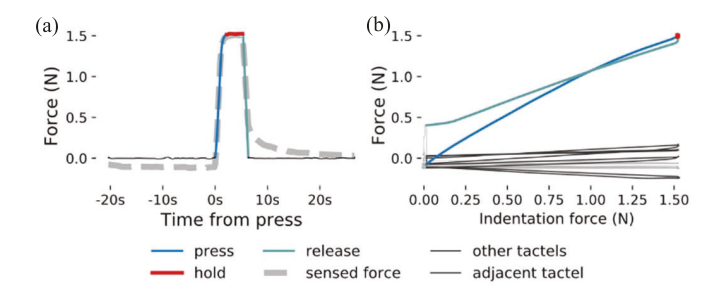


Fig. 14. (a) Indenter response identification in 1.5-N test for tactel #4. The dashed line represents sensor reading and the solid line represents indenter force feedback. (b) Hysteresis plot for tactel #4.

compare it synchronously to the collected sensor readings. The force baseline was established by leaving the system static for 30 s before engaging the indenter through a threshold higher than the baseline average. A Python script is developed to automatically identify a rising or falling edge on the force reading, corresponding to the sensor pressing or releasing. The relative flat region in between rising and falling edges is then identified as the force-holding phase and its average is calculated to calibrate the sensor reading.

Fig. 14(a) shows calibrated sensor readings and the indenter's force feedback when aligned on the same plot, while Fig. 14(b) shows hysteresis of sensor readings versus indenter force with excursions from 0 to 1.5 N of the same sensor. Data in Fig. 14 are shown for a sample Tactel #4, but it will look similar for the other functioning tactels. The baseline "zero" value for a tactel is the average when the indenter is not pressing. The calibration profile for each SkinCell tactel consists of three values: 1) a baseline value reading when the sensor tactel is "at rest" or not been pressed; 2) an average "active" reading when the tactel is pressed; and 3) the force in Newtons associated with this "active" state. We can see that as the tactel is pressed (blue), the sensor reading increases and remains steady in the hold region (red). As the indenter releases (cyan), the sensor value goes back down. The other gray plots in (b) show the behavior when other tactels were pressed, with adjacent tactels being slightly more highlighted in black.

The two streams of data representing indenter force and raw ADC readings are synchronized by their timestamps. For each calibration profile, we subtract the baseline value ("zero" calibration) and linearly scale the ADC readings based on sensitivity to force ("span" calibration). A linear relationship is used to describe the calibration

$$F(j) = a_j (v_j - b_j). (6)$$

In which the predicted force of tactel j, F(j), can be calculated from ADC's raw reading of v_j , with baseline adjustment b_j , and a linear coefficient a_j . For the moment, a linear model is used since the current sensor works best at small forces. It can be expanded to a quadratic model by adding a quadratic term. To summarize the sensitivity of one SkinCell sensor, the sensitivity profile of all sensor tactels from sample 1 except two malfunctioning ones is shown in Fig. 15(a). Sensor numbers 11, 12, 4, and 5 are chosen to represent the sensitivity

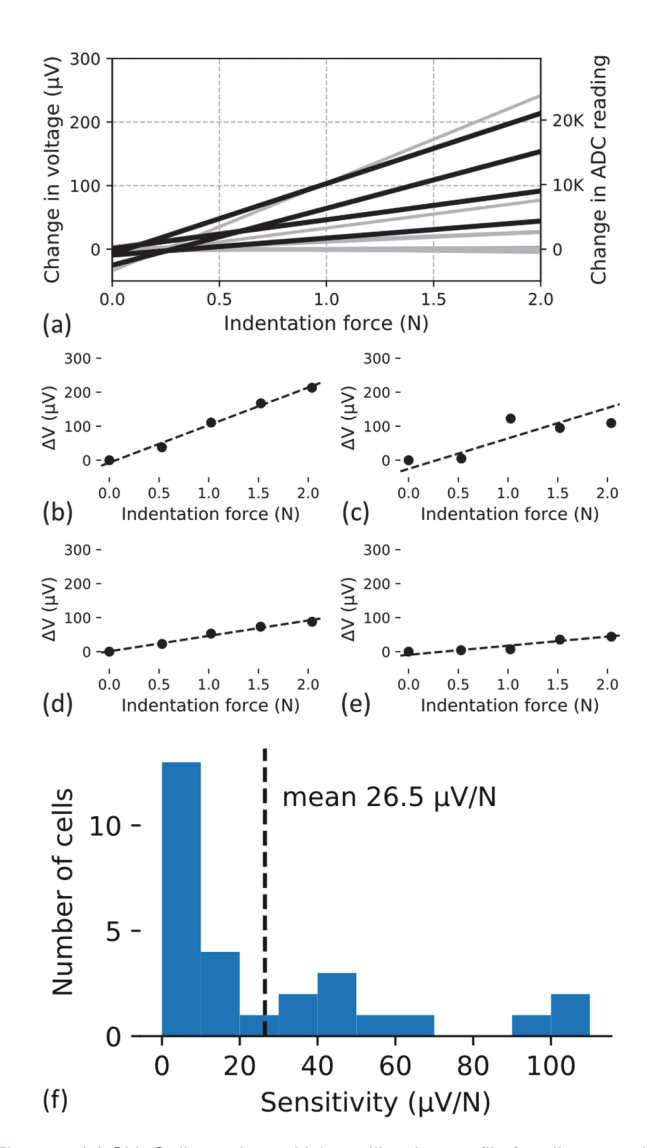


Fig. 15. (a) SkinCell tactel sensitivity calibration profile for all 16 tactels. The black lines indicate the profile for tactel #11, #12, #4, and #5 which indicate tactels have high sensitivity. (b)–(e) Individual linear fitting for sample tactels #11, #12, #4, and #5 with linear regression method. (f) Sensitivity variation of tactels from two sensor patches.

TABLE I
SKINCELL SENSITIVITY STATISTIC

	Average	Median	Minimum	Maximum	Std. Deviation
Sample 1	31.8	15.6	0.4	104.1	36.5
Sample 2	21.4	7.4	0.1	90.2	26.6
Overall	26.5	12.4	0.1	104.1	31.8

*Unit is μV/N.

spectrum of this patch. Fig. 15(f) shows a sensitivity histogram of two complete sensor patches. The range of sensitivities for our first sensor is 0.38–104.1 μ V/N, while the range of sensitivities for the second sensor array is 0.14–90.21 μ V/N. The yield on both sensors was 87.5%, meaning 14 out of 16 tactels are usable. The sensitivity statistic of the two patches is listed in Table I.

The experiment indicates the SkinCell sensors' sensitivity is roughly linear, as shown in Fig. 15(a)–(e), with respect

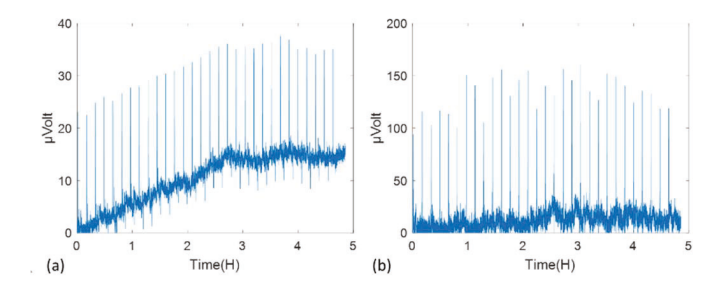


Fig. 16. (a) Tactel with severe drift and (b) tactel with minimum drift.

TABLE II
SKINCELL SENSOR BASELINE STABILITY

Average	Median	Minimum	Maximum	Std. Deviation
40.2%	27.6%	13.3%	83.3%	25.8

to the input force within the working range, which is 2 N. Wear and tear at the sensor pins were observed if the force input exceeds 6 N, and over time, it deteriorates the SkinCell performance. The range of 2-N force results A/D conversion of slightly higher than 20 000 readings according to Fig. 15(a), which is far away from saturating the 24-bit A/D conversion IC.

A 5-h continuous test was conducted to study the baseline stability of our tactile sensors under cyclic loading conditions. Our testing bench was programed for 2 N indentations with a 5-s hold time and 5-min release time across all 16 tactels. The purpose of the large release time was to ensure the elastomer relaxes to its original shape. Electronic responses from the tested SkinCell samples included a baseline of the sensor signal prior to each indentation which is compared to the original baseline before starting the cyclic test. The result shows an average baseline drift of 40.2% of the peak signal across 14 of the 16 working tactel of our tested SkinCell sensors. We believe the drift could be due to the slow sliding between the sensor patch and the encapsulation during the test. A representative response to this test is shown in Fig. 16 and summarized in Table II.

B. SkinCell Sensor Spatial Resolution Evaluation

One of the design goals of using silicone rubber encapsulation is to define the spatial resolution of SkinCell sensors. In this section, indentation experiments were conducted to evaluate spatial resolution.

Under the same testing bench as Section V-A, we applied 1-N force to a chosen tactel by indenters with spherical tips, and we also wanted to see that the responses are similar regardless of tip size. The first tip had an outer diameter of 3.9 mm and the second was 7.9 mm. We aligned the indenter to tactel #10 and then shifted the indenter ten times by steps of 0.7 mm toward $\pm X$ and $\pm Y$ directions, respectively (see Fig. 12). Thus, the last indentation aligns to an adjacent tactel to #10. The response at tactel #10 is shown in Fig. 17. The Y-axis represents the force reading in Newton, and the X-axis represents the experimental time in seconds. The first peak in

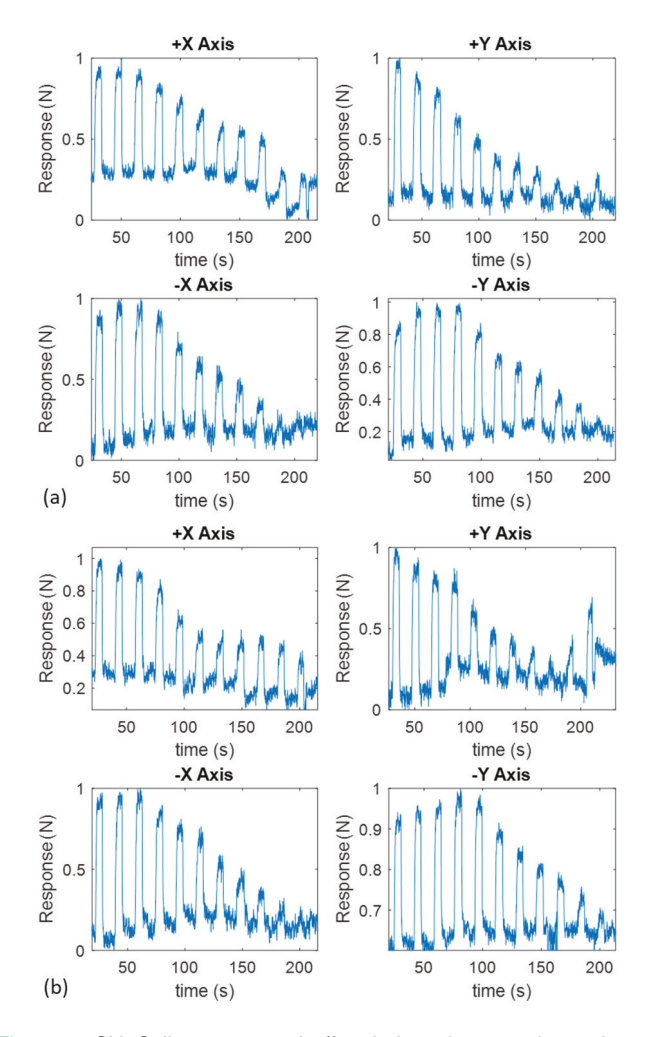


Fig. 17. SkinCell sensor tactel offset indentation experimental result for 1-N force loading. Results of indenter with (a) 3.9-mm diameter and (b) 7.9-mm diameter.

each plot represents aligned indentation on tactel #10, and the other peaks represent indentation at shifted locations.

Results indicate that tactel response starts to decay after the indenter moves away from the center of the tactel and becomes zero once the indenter reaches adjacent tactels in all directions. This effect is independent of indenter size and confirms that strain gauge SkinCell can be engineered to recover indenting force with the help of carefully designed encapsulation and calibration.

Baseline drift can also be observed from the results in Fig. 17. We believe this effect is due to the creep of the silicone material and the adhesive layers used in encapsulation [49]. A repetitive indentation in a short time slightly deforms the sensing region, which takes time to recover and creates baseline drift. Second, if too much force, beyond 6 N, is applied to the sensor, layers may shear and displace relative to the sensor, which can also cause baseline drift. In future iterative designs, we plan to improve sensor encapsulation alignment and adhesion, as well as reduce creep.

C. OctoCan Finger Indentation Experiment

A finger indentation experiment was conducted with a human subject applying force at random locations with their

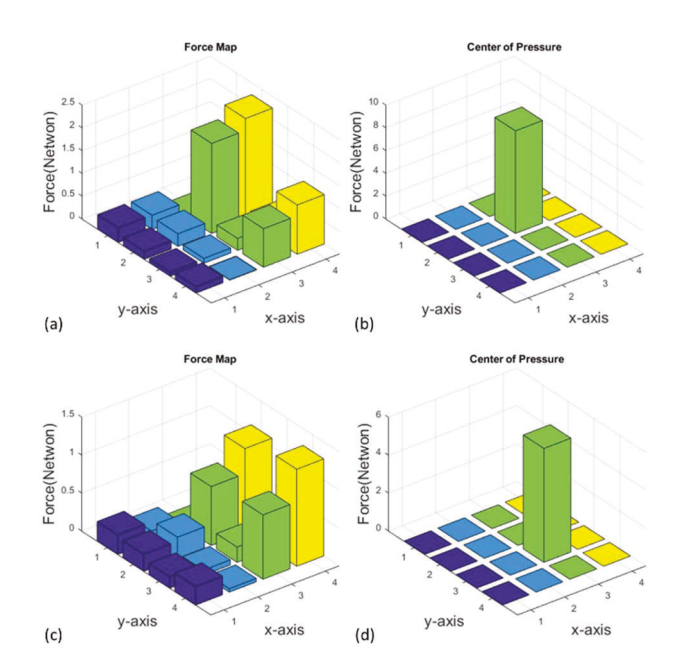


Fig. 18. (a) and (c) SkinCell sensor force map when a single finger is pressing, at two random moments. (b) and (d) Calculated the center of force of (a) and (c), respectively.

finger onto SkinCell sensors attached to the OctoCan controller. The collected data are then processed to create a force map to recover the contact force map, its resultant magnitude, and the center of pressure (COP) applied.

The calibrated sensitivity profiles were used to convert ADC voltage reading into force value on each tactel. Fig. 18(a) and (c) shows a reconstructed force map on one of the SkinCell sensors at moments that finger indentation has been detected, and Fig. 18(b) and (d) shows the calculated COP for (a) and (c) accordingly.

The COP of a sensor patch can be calculated by [29]

$$\vec{COP} = \frac{\sum_{j=1}^{N} F(j) \vec{c}_{j}}{\sum_{j=1}^{N} F(j)}$$
 (7)

where $\sum_{j=1}^{N} F(j)$ is the total force sensed across all the sensor tactels. By applying (7), the COP can be found for both experiments. In the case of Fig. 18(a), the COP is (2.3733, 3.2611) with a total force of 9 N, as shown in Fig. 18(b). The COP for Fig. 18(c) is (2.7686, 3.0830) and 6 N of the total force, as shown in Fig. 18(d).

VI. CONCLUSION

In this article, we have discussed the design, fabrication, and encapsulation of a SkinCell sensor patch, as well as the integration of 2 of these patches into the OctoCan for pHRI experiments. The SkinCell sensor incorporates 16 individual strain-gauge tactels and covers an area of 28×28 mm. Each tactel element measures 3.65 mm in diameter and 7 mm away from the other. A PDMS sensor encapsulation with strain concentration features has been designed to improve force sensing and define the spatial resolution of each sensor patch. FEA was conducted to confirm the sensitivity increase due to the encapsulation and the temperature compensation due to sensor lamination. An automatic testing bench was

employed to individually characterize the sensitivity of each tactel, and calibration profiles were generated. The average sensitivity of the sensor tactel is 26.5 μ V/N. The average yield of our fabrication process is 87.5%, which shows that our fabrication and encapsulation process is repeatable across samples but will need future optimization to reduce cell-to-cell variations. The effectiveness of the sensor encapsulation has been verified through spatial resolution experiments, which tactel responds similarly to force directly load on it and attenuates as indentation force moves away.

Finally, using the integration of SkinCell sensors into a structural electronic device OctoCan, we presented physical human finger indentation experiments. The experiment shows that interaction force map reconstruction and COP identification are possible for individual SkinCell sensors in contact with the human hand.

In the future, we will work to further improve the Skin-Cell sensor's force sensitivity as well as spatial resolution by employing additive manufacturing processes instead of cleanroom fabrication to reduce fabrication costs. The sensor patch encapsulation design also needs to be further studied so that the sensor generates optimal strain responses. The sensor patch tactel arrangement can also be revised to reduce the size of the OctoCan for better hand-grip ergonomics. The interconnect design will be improved to reduce substrate wear and tear when SkinCell sensors are exposed to force inputs higher than 6N. Finally, we plan to install the OctoCan onto a robotic arm and other mechatronic devices and conduct human–robot interaction experiments.

ACKNOWLEDGMENT

The authors extend their sincere appreciation for the help received from the Micro/Nano Technology Center staff during the fabrication process of our sensors. They also thank Saleh Khanjar, Kavish Sudan, and Douglas Jackson for their technical assistance with the experimental results presented in this article.

REFERENCES

- T. Yang, D. Xie, Z. Li, and H. Zhu, "Recent advances in wearable tactile sensors: Materials, sensing mechanisms, and device performance," *Mater. Sci. Eng. R, Rep.*, vol. 115, pp. 1–37, May 2017.
- [2] V. J. Lumelsky, M. S. Shur, and S. Wagner, "Sensitive skin," *IEEE Sensors J.*, vol. 1, no. 1, pp. 41–51, Jun. 2001.
- [3] R. S. Dahiya, G. Metta, M. Valle, and G. Sandini, "Tactile sensing-from humans to humanoids," *IEEE Trans. Robot.*, vol. 26, no. 1, pp. 1–20, Feb. 2010
- [4] G. Cheng, E. Dean-Leon, F. Bergner, J. R. G. Olvera, Q. Leboutet, and P. Mittendorfer, "A comprehensive realization of robot skin: Sensors, sensing, control, and applications," *Proc. IEEE*, vol. 107, no. 10, pp. 2034–2051, Oct. 2019.
- [5] J. Kuehn and S. Haddadin, "An artificial robot nervous system to teach robots how to feel pain and reflexively react to potentially damaging contacts," *IEEE Robot. Autom. Lett.*, vol. 2, no. 1, pp. 72–79, Jan. 2017.
- [6] C.-Y. Huang, W.-L. Sung, and W. Fang, "Develop and implement a novel tactile sensor array with stretchable and flexible grid-like spring," in *Proc. IEEE SENSORS*, Oct. 2017, pp. 1–3.
- [7] M. Sohgawa et al., "Fabrication and characterization of silicon-polymer beam structures for cantilever-type tactile sensors," in *Proc. TRANS-DUCERS Int. Solid-State Sensors, Actuat. Microsyst. Conf.*, Jun. 2007, pp. 1461–1464.
- [8] Y.-H. Jen et al., "Development and characterization of vertically stacked tactile sensor with hollow structure," *IEEE Sensors J.*, vol. 21, no. 5, pp. 5809–5818, Mar. 2021.

- [9] Y.-C. Liu, C.-M. Sun, L.-Y. Lin, M.-H. Tsai, and W. Fang, "Development of a CMOS-based capacitive tactile sensor with adjustable sensing range and sensitivity using polymer fill-in," *J. Microelectromech. Syst.*, vol. 20, no. 1, pp. 119–127, Feb. 2011.
- [10] S.-K. Yeh, J.-H. Lee, and W. Fang, "On the detection interfaces for inductive type tactile sensors," *Sens. Actuators A, Phys.*, vol. 297, Oct. 2019, Art. no. 111545.
- [11] S.-K. Yeh, C.-C. Ning, C.-Y. Yeh, S.-H. Tseng, Y.-Z. Juang, and W. Fang, "CMOS chip for solid-state tactile force sensor," in *Proc. IEEE SENSORS*, Oct. 2020, pp. 1–4.
- [12] S. K. Bahadir, "Identification and modeling of sensing capability of force sensing resistor integrated to e-textile structure," *IEEE Sensors J.*, vol. 18, no. 23, pp. 9770–9780, Dec. 2018.
- [13] D. J. Van Den Heever, K. Schreve, and C. Scheffer, "Tactile sensing using force sensing resistors and a super-resolution algorithm," *IEEE Sensors J.*, vol. 9, no. 1, pp. 29–35, Jan. 2009.
- [14] M. N. Saadatzi, J. R. Baptist, I. B. Wijayasinghe, and D. O. Popa, "Characterization of large-area pressure sensitive robot skin," *Proc. SPIE*, vol. 10216, May 2017, Art. no. 102160G.
- [15] Y. Tenzer, L. P. Jentoft, and R. D. Howe, "The feel of MEMS barometers: Inexpensive and easily customized tactile array sensors," *IEEE Robot. Autom. Mag.*, vol. 21, no. 3, pp. 89–95, Sep. 2014, doi: 10.1109/MRA.2014.2310152.
- [16] E. Donlon, S. Dong, M. Liu, J. Li, E. Adelson, and A. Rodriguez, "GelSlim: A high-resolution, compact, robust, and calibrated tactilesensing finger," in *Proc. IEEE/RSJ Int. Conf. Intell. Robots Syst. (IROS)*, Oct. 2018, pp. 1927–1934.
- [17] J. Li, S. Dong, and E. H. Adelson, "End-to-end pixelwise surface normal estimation with convolutional neural networks and shape reconstruction using GelSight sensor," in *Proc. IEEE Int. Conf. Robot. Biomimetics* (ROBIO), Dec. 2018, pp. 1292–1297.
- [18] R. Dahiya et al., "Large-area soft e-skin: The challenges beyond sensor designs," Proc. IEEE, vol. 107, no. 10, pp. 2016–2033, Oct. 2019.
- [19] J.-F. Lei and H. A. Will, "Thin-film thermocouples and strain-gauge technologies for engine applications," *Sens. Actuators A, Phys.*, vol. 65, pp. 187–193, Mar. 1998.
- [20] J. Tikka, R. Hedman, and A. Siljander, "Strain gauge capabilities in crack detection," in *Proc. Struct. Health Monit. Diagnosis Prognostics Struct. Health Manag., Proc. 4th Int. Workshop Struct. Health Monit.* Lancaster, PA, USA: DEStech Publications, 2003, pp. 15–17.
- [21] B. Kovačič, R. Kamnik, A. Štrukelj, and N. Vatin, "Processing of signals produced by strain gauges in testing measurements of the bridges," *Proc. Eng.*, vol. 117, pp. 795–801, Jan. 2015.
- [22] H. De Backer, W. De Corte, and P. Van Bogaert, "A case study on strain gauge measurements on large post-tensioned concrete beams of a railway support structure," *Insight-Non-Destructive Test. Condition Monit.*, vol. 45, no. 12, pp. 822–826, Dec. 2003.
- [23] J. G. Da Silva, A. A. De Carvalho, and D. D. Da Silva, "A strain gauge tactile sensor for finger-mounted applications," *IEEE Trans. Instrum. Meas.*, vol. 51, no. 1, pp. 18–22, Feb. 2002.
- [24] S. K. Das, M. N. Saadatzi, S. Abubakar, and D. O. Popa, "Joint torque estimation using base force-torque sensor to facilitate physical humanrobot interaction (pHRI)," in *Proc. IEEE 15th Int. Conf. Autom. Sci. Eng. (CASE)*, Aug. 2019, pp. 1367–1372.
- [25] J. R. Baptist, R. Zhang, D. Wei, M. N. Saadatzi, and D. O. Popa, "Fabrication of strain gauge based sensors for tactile skins," *Proc. SPIE*, vol. 10216, May 2017, Art. no. 102160F.
- [26] M. N. Saadatzi, Z. Yang, J. R. Baptist, R. R. Sahasrabud-dhe, I. B. Wijayasinghe, and D. O. Popa, "Parametric investigation of scalable tactile sensors," *Proc. SPIE*, vol. 10216, May 2017, Art. no. 102160A.
- [27] M. N. Saadatzi, S. K. Das, I. B. Wijayasinghe, D. O. Popa, and J. R. Baptist, "Precision grasp control with a pneumatic gripper and a novel fingertip force sensor," in *Proc. IEEE 14th Int. Conf. Autom. Sci. Eng. (CASE)*, Aug. 2018, pp. 1454–1459.
- [28] M. N. Saadatzi, J. R. Baptist, Z. Yang, and D. O. Popa, "Modeling and fabrication of scalable tactile sensor arrays for flexible robot skins," *IEEE Sensors J.*, vol. 19, no. 17, pp. 7632–7643, Sep. 2019.
- [29] S. Cremer, M. N. Saadatzi, I. B. Wijayasinghe, S. K. Das, M. H. Saadatzi, and D. O. Popa, "SkinSim: A design and simulation tool for robot skin with closed-loop pHRI controllers," *IEEE Trans. Autom. Sci. Eng.*, vol. 18, no. 3, pp. 1302–1314, Jul. 2021.
- [30] M. Bhattacharjee, M. Soni, P. Escobedo, and R. Dahiya, "PEDOT: PSS microchannel-based highly sensitive stretchable strain sensor," Adv. Electron. Mater., vol. 6, no. 8, 2020, Art. no. 2000445.

- [31] A. El Zein, C. Huppé, and C. Cochrane, "Development of a flexible strain sensor based on PEDOT: PSS for thin film structures," *Sensors*, vol. 17, no. 6, p. 1337, Jun. 2017.
- [32] B. Thompson and H. Yoon, "Aerosol-printed strain sensor using PEDOT: PSS," *IEEE Sensors J.*, vol. 13, no. 11, pp. 4256–4263, Nov. 2013, doi: 10.1109/JSEN.2013.2264482.
- [33] I. D. Johnston, D. K. McCluskey, C. K. L. Tan, and M. C. Tracey, "Mechanical characterization of bulk Sylgard 184 for microfluidics and microengineering," *J. Micromech. Microeng.*, vol. 24, no. 3, Mar. 2014, Art. no. 035017.
- [34] Y. Zhang and N. Miki, "Sensitivity enhancement of a micro-scale biomimetic tactile sensor with epidermal ridges," *J. Micromech. Microeng.*, vol. 20, no. 8, Aug. 2010, Art. no. 085012.
- [35] K. Kim et al., "Polymer-based flexible tactile sensor up to 32×32 arrays integrated with interconnection terminals," *Sens. Actuators A, Phys.*, vol. 156, no. 2, pp. 284–291, Dec. 2009.
- [36] W.-C. Choi, "Polymer micromachined flexible tactile sensor for three-axial loads detection," *Trans. Elect. Electron. Mater.*, vol. 11, no. 3, pp. 130–133, Jun. 2010.
- [37] Y.-F. Wang et al., "Fully printed PEDOT: PSS-based temperature sensor with high humidity stability for wireless healthcare monitoring," Sci. Rep., vol. 10, no. 1, p. 2467, Dec. 2020.
- [38] D. Wei, R. Zhang, M. N. Saadatzi, O. O. Olowo, and D. Popa, "Organic piezoresistive pressure sensitive robotic skin for physical human–robot interaction," in *Proc. Int. Design Eng. Tech. Conf. Comput. Inf. Eng. Conf., 14th Int. Conf. Micro Nanosyst. (MNS).* vol. 1, Aug. 2020, Art. no. V001T01A013.
- [39] O. O. Olowo, R. Zhang, Z. Yang, B. Goulet, and D. O. Popa, "Organic piezoresistive robotic skin sensor fabrication, integration and characterization," in *Proc. 16th Int. Manuf. Sci. Eng. Conf. Manuf. Processes Manuf. Syst., Nano/Micro/Meso Manuf., Quality Rel.*, vol. 2, Jun. 2021, Art. no. V002T08A013.
- [40] Sigma-Aldrich. (2020). MIllipore Sigma. Accessed: Jan. 26, 2020. [Online]. Available: https://www.sigmaaldrich.com/catalog/product/aldrich/655201?lang=en®ion=U.S
- [41] J. Engel, J. Chen, and C. Liu, "Development of polyimide flexible tactile sensor skin," *J. Micromech. Microeng.*, vol. 13, no. 3, pp. 359–366, May 2003.
- [42] X. Sun et al., "Recent applications of different microstructure designs in high performance tactile sensors: A review," *IEEE Sensors J.*, vol. 21, no. 9, pp. 10291–10303, May 2021, doi: 10.1109/JSEN.2021.3061677.
- [43] T. Teranishi, H. Hirano, and S. Tanaka, "Tactile sensing from backside of flexible printed circuit using LSI-integrated sensor with elastic dome structure," in *Proc. 20th Int. Conf. Solid-State Sensors, Actuat. Microsyst. Eurosensors XXXIII* (TRANSDUCERS EUROSENSORS XXXIII), Jun. 2019, pp. 547–550, doi: 10.1109/TRANSDUCERS.2019.8808705.
- [44] C. Cochrane, V. Koncar, M. Lewandowski, and C. Dufour, "Design and development of a flexible strain sensor for textile structures based on a conductive polymer composite," *Sensors*, vol. 7, no. 4, pp. 473–492, Apr. 2007, doi: 10.3390/s7040473.
- [45] N. Trifigny, F. Kelly, C. Cochrane, F. Boussu, V. Koncar, and D. Soulat, "PEDOT: PSS-based Piezo-resistive sensors applied to reinforcement glass fibres for in situ measurement during the composite material weaving process," *Sensors*, vol. 13, no. 8, pp. 10749–10764, Aug. 2013, doi: 10.3390/s130810749.
- [46] L. F. Francis, J. C. Grunlan, J. Sun, and W. W. Gerberich, "Conductive Coatings from latex-based dispersions," in *Proc. 12th Int. Coating Sci. Technol. Symp.*, Rochester, NY, USA, Sep. 2004, pp. 184–185.
- [47] S. Yang and N. Lu, "Gauge factor and stretchability of siliconon-polymer strain gauges," *Sensors*, vol. 13, no. 7, pp. 8577–8594, Jul. 2013.
- [48] G. Latessa, F. Brunetti, A. Reale, G. Saggio, and A. Di Carlo, "Piezoresistive behaviour of flexible PEDOT: PSS based sensors," Sens. Actuators B, Chem., vol. 139, no. 2, pp. 304–309, Jun. 2009.
- [49] F. Schneider, T. Fellner, J. Wilde, and U. Wallrabe, "Mechanical properties of silicones for MEMS," *J. Micromech. Microeng.*, vol. 18, no. 6, Jun. 2008, Art. no. 065008.
- [50] D. Lei et al., "Research progress of MXenes-based wearable pressure sensors," APL Mater., vol. 8, no. 11, Nov. 2020, Art. no. 110702.
- [51] Y. Guo, M. Zhong, Z. Fang, P. Wan, and G. Yu, "A wearable transient pressure sensor made with Mxene nanosheets for sensitive broad-range human–machine interfacing," *Nano Lett.*, vol. 19, no. 2, pp. 1143–1150, 2019.
- [52] S.-K. Kang et al., "Bioresorbable silicon electronic sensors for the brain," *Nature*, vol. 530, pp. 71–76, Jan. 2016.

- [53] A. Palmroth, T. Salpavaara, J. Lekkala, and M. Kellomäki, "Fabrication and characterization of a wireless bioresorbable pressure sensor," Adv. Mater. Technol., vol. 4, no. 9, Sep. 2019, Art. no. 1900428.
- [54] N. Liu, G. Fang, J. Wan, H. Zhou, H. Long, and X. Zhao, "Electro-spun PEDOT: PSS–PVA nanofiber based ultrahigh-strain sensors with controllable electrical conductivity," *J. Mater. Chem.*, vol. 21, no. 47, pp. 18962–18966, 2011.
- [55] J. A. Florez and A. Velasquez, "Calibration of force sensing resistors (FSR) for static and dynamic applications," in *Proc. IEEE ANDESCON*, Sep. 2010, pp. 1–6, doi: 10.1109/ANDESCON.2010.5633120.
- [56] L. Paredes-Madrid, C. Palacio, A. Matute, and C. P. Vargas, "Underlying physics of conductive polymer composites and force sensing resistors (FSRs) under static loading conditions," *Sensors*, vol. 17, no. 9, p. 2108, Sep. 2017, doi: 10.3390/s17092108.
- [57] I. Graz et al., "Flexible active-matrix cells with selectively poled bifunctional polymer-ceramic nanocomposite for pressure and temperature sensing skin," *J. Appl. Phys.*, vol. 106, no. 3, Aug. 2009, Art. no. 034503, doi: 10.1063/1.3191677.
- [58] D. Silvera-Tawil, D. Rye, and M. Velonaki, "Artificial skin and tactile sensing for socially interactive robots: A review," *Robot. Auton. Syst.*, vol. 63, no. 3, pp. 230–243, Jan. 2015.
- [59] L. Yang et al., "Wearable pressure sensors based on MXene/tissue papers for wireless human health monitoring," ACS Appl. Mater. Interfaces, vol. 13, no. 50, pp. 60531–60543, Dec. 2021.
- [60] J. A. Paulsen, M. Renn, K. Christenson, and R. Plourde, "Printing conformal electronics on 3D structures with aerosol jet technology," in Proc. Future Instrum. Int. Workshop (FIIW) Proc., Oct. 2012, pp. 8–9.
- [61] J. Engel, J. Chen, Z. Fan, and C. Liu, "Polymer micromachined multimodal tactile sensors," *Sens. Actuators A, Phys.*, vol. 117, no. 1, pp. 50–61, Jan. 2005.



Ruoshi Zhang (Member, IEEE) was born in China, in 1989. He received the B.S. degree in telecommunication engineering from Tianjin University Ren'ai College, Tianjin, China, in 2012, the M.S. degree in electrical engineering from the University of Texas at Arlington, Arlington, TX, USA, in 2015, and the Ph.D. degree in electrical engineering from the University of Louisville, Louisville, KY, USA, in 2020.

From 2016 to 2020, he was a Research Assistant with the Next Generation System Group

(NGS), University of Louisville, where he has been a Postdoctoral Associate with the Electrical and Computer Engineering Department since 2020. He has published two journal papers and more than ten conference papers. His research interest includes sensor technology, microtechnology, robotics, and embedded systems.

Dr. Zhang received the Best Student Paper Award twice at IEEE International Conference on Manipulation, Automation and Robotics at Small Scales, in 2018 and 2019.

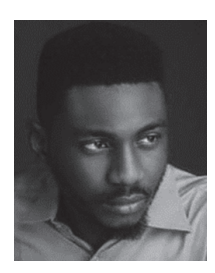


Ji-Tzuoh Lin was born in Taipei, Taiwan. He received the M.S. degree in physics and the Ph.D. degree in electrical engineering from the University of Louisville, Louisville, KY, USA, in 2000 and 2006, respectively. His Ph.D. study was to develop MEMS spinal fusion sensors and their telemetry system.

He is a Research Engineer with the Louisville Automation and Robotic Research Institution (LARRI), University of Louisville. He had started a company, Ambiharv, Louisville, Kentucky.

He has one issued patent, two book chapters, and more than 20 peerreviewed journal publications. After graduation, he extended his research interests to MEMS devices that enable small-scale vibrational energy harvesting and micro-explosion. During the past few years, the focus was turned to radiation detection with MEMS resonators for space application. He is currently working on research involving optical time of flight (TOF) sensors and polymer strain gauges. Both areas will be used for human interfaces for location and environmental detection.

Dr. Lin received the SBIR Award. He was placed first in the student competition in the medical and engineering category in research, Louisville, in 2004. His paper "Magnetic coupling of the piezoelectric cantilever for enhanced energy harvesting efficiency" was selected by *Smart Materials and Structure* to the collection of the journal's highlight of the year 2010. Another paper "Thermal Response and TC f of GaN/AIN Heterostructure Multimode Micro String Resonators From $-10~^{\circ}\text{C}$ Up to 325 $^{\circ}\text{C}$ " was highlighted in the August 2021 issue of Journal of Microelectromechanical Systems (JMEMS).



Olalekan O. Olowo received the B.Sc. degree in electrical and electronics engineering from Ekiti State University, Ado Ekiti, Nigeria, in 2013, and the master's degree in electrical and electronic engineering from Covenant University, Ota, Ogun, Nigeria, in 2017. He is currently pursuing the Ph.D. degree in electrical and computer engineering with the University of Louisville, Louisville, KY, USA.

Since 2019, he has been a Graduate Research Assistant with the Louisville Automation Robotics

and Research Institute, Louisville. His research interests include power system engineering, fiber Bragg grating, micro-nanostructures, and fabrication and integration of robot skin sensor.

Mr. Olowo was a recipient of the Kentucky National Science Foundation EPSCOR "Mark of Distinction" Award in 2020.



Bryan Harris received the B.S. and M.Eng. degrees in computer engineering and computer science from the University of Louisville, Louisville, KY, USA, in 2017 and 2018, respectively, where he is currently pursuing the Ph.D. degree in computer science and engineering.

Since 2018, he has been a Research Assistant with the Computer Systems Laboratory and the Louisville Automation and Robotics Research Institute (LARRI), Louisville. His research interests include data storage systems, operating

system design, parallel and distributed systems, and high-performance computing.



Brian P. Goulet was born in Columbia, MD, USA, in 1997. He received the B.S. degree in electrical and computer engineering from the University of Louisville, Louisville, KY, USA, in 2020, where he is currently pursuing the M.S. degree in electrical engineering.

From 2019 to 2020, he was an Undergraduate Research Assistant with the University of Louisville, where he has continued his research as a Graduate Research Assistant with the NGS Group. His research interests include the devel-

opment of control systems for characterizing and testing sensors to better future development.



Dan O. Popa (Senior Member, IEEE) received the B.A. degree in engineering, mathematics, and computer science and the M.S. degree in engineering from Dartmouth College, Hanover, NH, USA, in 1993 and 1994, respectively, and the Ph.D. degree in EE from the Rensselaer Polytechnic Institute (RPI), Troy, NY, USA, in 1998, focusing on motion planning for nonholonomic robots.

In 1998, he joined the Center for Automation Technologies, RPI, where he held the rank of

Senior Research Scientist. In 2004, he became an Assistant Professor and then an Associate Professor of Electrical Engineering at The University of Texas at Arlington, Arlington, TX, USA, until 2015. Since 2016, he has been the Vogt Endowed Chair in advanced manufacturing and a Professor of Electrical and Computer Engineering with the University of Louisville, Louisville, KY, USA, where he is currently the Head of the Next Generation Research Group (NGS), and the Director of the Louisville Automation and Research Institute (LARRI), conducting research in two main areas: the design, characterization, modeling, and control of micro actuators and precision robots and social and physical human—robot interaction through adaptive interfaces and robot skin. He is the author of over 200 refereed conference and journal papers and book chapters published with the IEEE and ASME societies.

Dr. Popa was a recipient of several prestigious awards.